

This is the accepted manuscript made available via CHORUS. The article has been published as:

Oxygen evolution from olivine $\text{Mn}_{1-x}\text{M}_x\text{PO}_4$
($\text{M}=\text{Fe}, \text{Ni}, \text{Al}, \text{Mg}$) delithiated cathode materials

David H. Snyder and C. Wolverton

Phys. Rev. B **95**, 024102 — Published 3 January 2017

DOI: [10.1103/PhysRevB.95.024102](https://doi.org/10.1103/PhysRevB.95.024102)

Oxygen Evolution from Olivine $\text{Mn}_{1-x}\text{M}'_x\text{PO}_4$
($\text{M}' = \text{Fe}, \text{Ni}, \text{Al}, \text{Mg}$) Delithiated Cathode Materials

David H. Snyder and C. Wolverton

Dept. of Materials Science and Engineering, Northwestern University

2220 Campus Drive, Evanston, IL 60208

ABSTRACT

Olivine LiMnPO_4 is a promising cathode material for Li-ion batteries. One drawback of this material is the propensity of its delithiated phase, MnPO_4 , to evolve oxygen gas above approximately 200 °C. During thermal runaway of cells, this oxygen gas can burn the electrolyte and other cell components and thereby jeopardize safety. Partial substitution of Mn with $\text{M}' = \text{Fe, Ni, Al, or Mg}$ has been used to improve the lithium intercalation kinetics of Li_xMnPO_4 ; however, the effect of these substitutions on oxygen evolution is not fully documented. In this paper, we calculate phase diagrams and oxygen evolution diagrams for these $\text{Mn}_{1-x}\text{M}'_x\text{PO}_4$ delithiated cathode materials. To generate the phase diagrams, we use sub-regular solid solution models and fit the energetic parameters of these models to density functional theory calculations of special quasi-random structures. The resulting thermodynamic models describe the effect of mixing on the initial temperature of oxygen evolution and on the cumulative amount of oxygen evolution at elevated temperatures. We find that addition of Fe increases the initial temperature and decreases the cumulative amount of oxygen evolution. $\text{Mn}_{0.5}\text{Fe}_{0.5}\text{PO}_4$ exhibits an initial temperature 50 °C higher than MnPO_4 and releases 70% less oxygen gas at 300 °C. Al is insoluble in MnPO_4 , so addition of Al has no effect on the initial temperature. However, Al addition does slightly decrease the amount of oxygen evolution due to an inactive AlPO_4 component. Mg and Ni both decrease the initial temperature of oxygen evolution, and therefore may worsen the safety of MnPO_4 .

I. INTRODUCTION

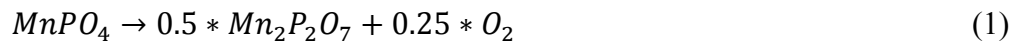
Portable electronics and electric vehicles require batteries with high energy density and thermal safety. Li-ion batteries are dominating these markets using a variety of existing cathode

materials, and new cathode materials are being developed to improve performance.¹ Each cathode material offers a balance of safety, energy density, and other attributes. Certain cathode materials jeopardize safety at elevated temperatures through oxygen evolution. Oxygen in the cell can contribute to fires and explosions through combustion of the organic electrolyte.

Olivine LiFePO₄ has demonstrated excellent safety due, in part, to a lack of oxygen evolution from its delithiated FePO₄ phase at temperatures up to 500 °C.² LiFePO₄ also delivers exceptional lifespan due to the metastability of FePO₄ in the olivine structure.^{3,4} However, LiFePO₄ suffers from relatively low energy density due to its low voltage at 3.4 V.⁵ To increase the voltage of olivine cathodes, Fe can be substituted with Mn.

LiMnPO₄ also forms the olivine structure and provides a voltage of 4.1 V.⁵ However, this material suffers from poor kinetics and oxygen evolution. Kinetics have been improved by mixing metals (M') such as Fe, Ni, Al, and Mg on the Mn sublattice to form mixed LiMn_{1-x}M'_xPO₄ materials, which also form the olivine structure.⁶ Beyond kinetics, a remaining problem for LiMnPO₄ cathodes is oxygen evolution from the delithiated olivine MnPO₄ phase that forms in the cell during charging.

Charging of LiMnPO₄ operates via a two-phase reaction where lithiated LiMnPO₄ and delithiated MnPO₄ phases coexist.⁷ The LiMnPO₄ phase is thermally stable up to at least 800 °C;⁸ however, the delithiated MnPO₄ phase releases oxygen gas above approximately 200 °C. This gas release occurs with the formation of Mn₂P₂O₇ according to experimental studies.⁹⁻¹¹



It is possible to control oxygen evolution from delithiated cathode materials by synthesizing the materials with various mixtures of transition metals.¹² For example, mixing metals such as Fe onto the Mn sublattice can stabilize the delithiated phase relative to product phases (e.g., Eq. 1),

and therefore improve oxygen evolution behavior.¹³ Inversely, metals that stabilize product phases can worsen oxygen evolution. Metals may be added to purposefully control oxygen evolution behavior, or they may be added to control kinetic or other properties with unintended consequences for oxygen evolution. In any case, it is important to understand the relationship between composition and oxygen evolution.

Experimental studies have characterized oxygen evolution from mixed $\text{Mn}_{1-x}\text{Fe}_x\text{PO}_4$ materials, finding initial temperatures of oxygen evolution between those of the pure MnPO_4 and FePO_4 end-members.^{13,14} However, these experimental $\text{Mn}_{1-x}\text{Fe}_x\text{PO}_4$ studies have arrived at varying conclusions at least partly due to a lack of well-established phase diagrams for these delithiated mixed-metal phases. Therefore, computational studies are useful for providing additional understanding of $\text{Mn}_{1-x}\text{Fe}_x\text{PO}_4$ phase diagrams. Furthermore, the effect on oxygen evolution of mixing other metals such as $\text{M}' = \text{Ni}, \text{Al}, \text{and Mg}$ in $\text{Mn}_{1-x}\text{M}'_x\text{PO}_4$ has not been previously reported to our knowledge. Density functional theory (DFT) calculations can be used to study delithiated cathode materials that are formed in batteries and therefore difficult to characterize with experimental techniques.¹⁵⁻¹⁸ Following the advent of modern computational resources, a large number of DFT papers have been published on technologically important materials including lithium-ion cathode materials.¹⁹⁻²⁴ DFT calculations on pure MnPO_4 have corroborated $\text{Mn}_2\text{P}_2\text{O}_7$ formation, but these calculations have not yet been extended to mixed $\text{Mn}_{1-x}\text{M}'_x\text{PO}_4$ cathodes.²⁵

In this paper, we use DFT and calculation of phase diagram (CALPHAD) methods to calculate mixing energies, phase diagrams, and oxygen evolution diagrams for delithiated $\text{Mn}_{1-x}\text{M}'_x\text{PO}_4$ olivine materials with $\text{M}' = \text{Fe}, \text{Ni}, \text{Al}, \text{and Mg}$. For various cathode compositions, we determine the temperature at which oxygen evolution initiates (T_{O_2}) and the cumulative amount

of oxygen released from the cathode (δ) as a function of temperature. We find that Fe mixing can both increase T_{O_2} and decrease δ . For example, $Mn_{0.5}Fe_{0.5}PO_4$ exhibits a T_{O_2} that is 50 °C higher than $MnPO_4$ and decreases δ by 70% at 300 °C. We find that Al mixing has no effect on T_{O_2} and decreases δ only in proportion to the degree of Al substitution. We find that Ni and Mg mixing decrease T_{O_2} but have no effect on δ . Within our study, metals that tend to adopt 2+ oxidation states in phosphates such as Ni and Mg worsen oxygen evolution behavior; whereas, 3+ metals such as Fe and Al can sometimes but not always improve oxygen evolution behavior. These findings help clarify the effect of transition metal mixing on oxygen evolution and therefore facilitate simultaneous optimization of performance and safety.

II. METHODOLOGY

We performed DFT calculations using the Vienna Ab-initio Simulation Package (VASP).²⁶⁻²⁹ We used projector augmented wave potentials^{30,31} and the PBE³² exchange-correlation functional. We use an energy cutoff of 520 eV and k-points of 1,000 per reciprocal atom, which results in DFT formation energies converged within 3 meV per formula unit. A DFT+U³³⁻³⁵ correction was applied to transition metal atoms using the method of Dudarev et al.³⁶ U values were taken from the paper by Wang et al., where they were fit to experimental oxide formation energies.³⁷ This paper by Wang et al. provides extensive discussion regarding the relationship between U values and oxide formation energies, and validates the DFT+U method for studying oxygen evolution reactions. The U values in eV are $U_{Mn} = 3.8$, $U_{Fe} = 4.0$, and $U_{Ni} = 6.4$. These are the same U values used in the Open Quantum Materials Database (OQMD), which provided a library of crystal structures as described below.^{17,38} Calculations were spin polarized, and transition metals were initialized in ferromagnetic configurations with +5 μ_B

magnetic moments. All calculations containing Ni were additionally run with Ni atoms in $+1 \mu_B$ initial magnetic moments to facilitate convergence toward low spin states.

To describe thermodynamics of mixing, we used a sub-regular solution model for the free energies of $\text{Mn}_{1-x}\text{M}'_x\text{PbO}_c$ ($0 < x < 1$) phases with binary mixing:

$$G(x, T) = H(x) + k_B T * [(x) \ln(x) + (1 - x) \ln(1 - x)] \quad (2)$$

In the sub-regular solution model, $H(x)$ is a third-order Redlich-Kister polynomial for the enthalpy.

$$H(x) = x(1 - x)L_0 + x(1 - x)(2x - 1)L_1 \quad (3)$$

L_0 is the regular solution parameter, and L_1 is the sub-regular solution parameter. $H(x)$ was fit to DFT mixing energies calculated for special quasi-random structures (SQSs), which are specially-constructed small unit cells that mimic the short-range pair and multi-body correlations of random solid solutions.³⁹ We used SQSs at $x = 0.25, 0.5$, and 0.75 compositions, and we generated these SQSs with the Monte-Carlo SQS (MCSQS) generator provided in the Alloy Theoretic Automated Toolkit (ATAT).⁴⁰ This approach followed previous work by Snyderaker and Wolverton on the phase diagrams of $\text{Li}_y\text{Mn}_{1-x}\text{Fe}_x\text{PO}_4$ and $\text{Li}_y\text{Mn}_{1-x}\text{Ni}_x\text{PO}_4$, which showed that these phases form mixed-metal solid solutions.⁴¹ We modeled solid solutions for all crystal structures (not only olivine) that appeared on the DFT convex hull at compositions of $\text{Mn}_{1-x}\text{M}'_x\text{PO}_4$ ($\text{M}' = \text{Fe}, \text{Ni}, \text{Al}, \text{and Mg}$) for oxygen chemical potentials corresponding to a range of temperatures between 0 K and 1,500 K. We used the DFT convex hulls of both the Open Quantum Materials Database (OQMD)^{38,42} and the Materials Project⁴³⁻⁴⁵ database. These databases provided similar convex hulls, except for the $\text{Fe}_3\text{P}_4\text{O}_{14}$ and $\text{Fe}_7\text{P}_6\text{O}_{24}$ compounds, which had large primitive cells and appeared only the Materials Project database. All solid phases that appear on the convex hulls at the $\text{Mn}_{1-x}\text{M}'_x\text{PO}_4$ compositions are ternary $\text{M}_a\text{P}_b\text{O}_c$

phases with $M = \text{Mn, Fe, Ni, Al, or Mg}$. Within this set of phases, each unique crystal structure was modeled as a $\text{Mn}_{a-a*x}\text{M}'_{a*x}\text{P}_b\text{O}_c$ ($0 < x < 1$) solid solution with $M' = \text{Ni, Fe, Al, or Mg}$.

We combined our DFT free energies of compounds and mixed solid-solution phases with a temperature-dependent oxygen chemical potential. We expressed the free energy of oxygen gas as a function of temperature, using data from the JANAF Thermochemical tables.⁴⁶ The free energy of oxygen gas was fit to reproduce the experimentally observed 200°C (473 K) initial temperature for oxygen evolution from MnPO_4 .⁹⁻¹¹ In these experiments, no partial pressure for oxygen gas is reported. We assumed an oxygen partial pressure of 1.0 bar. During thermal runaway of a lithium-ion cell with a cylindrical 18650 form factor and a $\text{Li}_x\text{Mn}_{1/3}\text{Co}_{1/3}\text{Ni}_{1/3}\text{O}_2$ cathode, the generation of oxygen, carbon dioxide, and other gases can increase total pressure up to approximately 10 bar.⁴⁷ Therefore, we also considered an oxygen partial pressure of 10 bar. However, we found that increasing oxygen partial pressure to 10 bar did not have a significant effect on our calculated results, so we only report results for 1.0 bar. Oxygen evolution from MnPO_4 occurs according to the reaction shown in Equation 1, which was used to set the chemical potential of oxygen gas at 473 K:

$$\mu_O^{473K} = E^{DFT}[2 * \text{MnPO}_4] - E^{DFT}[\text{Mn}_2\text{P}_2\text{O}_7] \quad (4)$$

E^{DFT} are DFT energies. The temperature-dependence of the JANAF data was then calibrated to this reference chemical potential, μ_O^{473K} . This approach allowed us to calculate oxygen evolution temperatures for $\text{Mn}_{1-x}\text{M}'_x\text{PO}_4$ materials relative to the experimental oxygen evolution temperature for MnPO_4 , independent of DFT errors for O_2 .^{37,48} Prior DFT papers have fit oxygen chemical potentials to formation energies of oxides,^{37,48} but in this paper, we fit oxygen chemical potentials to the $\text{MnPO}_4 \rightarrow \text{Mn}_2\text{P}_2\text{O}_7$ transition to provide accuracy specifically for phosphates.

The free energy functions for the solid solution phases and oxygen gas formed the thermodynamic database for phase diagram calculations. We use the Thermo-Calc software package to calculate phase diagrams.⁴⁹ Within Thermo-Calc, we input our DFT-derived free energies into the Gibbs module. We created phase diagrams for the binary systems defined by $\text{Mn}_{1-x}\text{M}'_x\text{PO}_4$ ($\text{M}' = \text{Fe}, \text{Ni}, \text{Al}, \text{Mg}$). Thermo-Calc settings are described in the Appendix.

Each phase diagram was calculated by considering all solid solution phases during energy minimization, with one exception. For the Mn-Fe system, we produced one phase diagram that included all phases, and another phase diagram that excluded the quartz-type ($\text{P3}_1\text{2}_1$) FePO_4 phase. For FePO_4 , the quartz-type phase gives a lower DFT energy than the olivine phase.²⁵ During synthesis, the quartz-type phase also forms preferentially to olivine.⁵⁰ However, the quartz-type FePO_4 phase is kinetically inaccessible in Li-ion cells with olivine FePO_4 delithiated cathodes.⁵¹ Furthermore, experiments have shown that olivine $\text{Mn}_{1-x}\text{Fe}_x\text{PO}_4$ phases also do not convert to quartz-type at elevated temperatures.¹⁴ Therefore, we are mainly interested in oxygen evolution from the olivine phase and chose to generate a phase diagram that excluded the quartz-type phase. This approach is consistent with prior DFT studies on oxygen evolution from FePO_4 , which report phase diagrams alternatively excluding and including the quartz-type phase.²⁵

Oxygen evolution from the cathode materials can be quantified using two metrics. The first metric is the initial temperature of oxygen evolution (T_{O_2}), which is the threshold temperature where oxygen is first released (at 1 bar) from the cathode during heating. Once this initial temperature is crossed, the released oxygen can burn the electrolyte and continue raising the temperature. The second metric is the cumulative amount of oxygen gas released at 1 bar from the cathode at any given temperature (δ). We define δ according to the $\text{MPO}_{4-\delta}$

composition of solid phases in the cathode. In this notation, a composition of $\text{MPO}_{4-\delta}$ implies a set of phases that sum to an overall composition of $\text{MPO}_{4-\delta}$. In this paper, both T_{O_2} and δ are defined at stable thermodynamic equilibrium.

We generated oxygen evolution diagrams using equilibria calculated in Thermo-Calc. For pure MnPO_4 , these oxygen evolution diagrams represent the decomposition reaction to form $\text{Mn}_2\text{P}_2\text{O}_7$, which is shown above in Equation 1. For mixed the $\text{Mn}_{1-x}\text{M}'_x\text{PO}_4$ materials, the oxygen evolution diagrams represent generalized decomposition reactions whose products are the equilibrium phases specified by the phase diagrams. We calculated equilibrium phases for an array of different composition and temperature conditions. The amounts of oxygen gas in these equilibrium calculations were used to create the oxygen evolution diagrams. We report oxygen evolution in terms of δ from $\text{MPO}_{4-\delta}$. We also report mass retention, which is expressed as a percentage of the mass of the $\text{Mn}_{1-x}\text{M}'_x\text{PO}_4$ material. For the redox active metals Fe and Ni, which are typically used in cathodes at high concentrations, we generated oxygen evolution diagrams over a full range: $0 < x < 1$ in $\text{Mn}_{1-x}\text{M}'_x\text{PO}_4$. For the redox inactive dopants Al and Mg, which are typically used in cathodes at low concentrations, we generated oxygen evolution diagrams over a narrower range: $0 < x < 0.2$ in $\text{Mn}_{1-x}\text{M}'_x\text{PO}_4$.

III. RESULTS AND DISCUSSION

We identified ten unique phases on the DFT convex hulls for $\text{Mn}_{1-x}\text{M}'_x\text{PO}_4$ ($\text{M}' = \text{Fe}, \text{Ni}, \text{Al}, \text{and Mg}$) compositions with oxygen chemical potentials corresponding to temperatures between 0 K and 1,500 K. These phases were used for solid solution modeling and calculation of phase diagrams. All phases on the DFT convex hulls, except for oxygen gas, contained either Mn or M' and contained both P and O. We identified two Mn-containing phases: MnPO_4

(Pnma) and $\text{Mn}_2\text{P}_2\text{O}_7$ (C2/m). We found five Fe-containing phases: FePO_4 (P3_12_1), $\text{Fe}_2\text{P}_2\text{O}_7$ ($\text{P}\bar{1}$), $\text{Fe}_3\text{P}_2\text{O}_8$ ($\text{P2}_1/\text{c}$), $\text{Fe}_3\text{P}_4\text{O}_{14}$ (Pnma), and $\text{Fe}_7\text{P}_6\text{O}_{24}$ ($\text{P}\bar{1}$). We also found $\text{Ni}_2\text{P}_2\text{O}_7$ ($\text{P2}_1/\text{c}$), AlPO_4 (P3_12_1), and $\text{Mg}_2\text{P}_2\text{O}_7$ (C2/m). $\text{Mn}_2\text{P}_2\text{O}_7$ and $\text{Mg}_2\text{P}_2\text{O}_7$ share the same C2/m space group. FePO_4 and AlPO_4 have many polymorphs within 10 meV/atom of the convex hull, including the shared P3_12_1 (quartz-type) structure, which is observed experimentally for both compositions. Therefore, the P3_12_1 structure was used for solid solution modeling of the FePO_4 and AlPO_4 phases. The ten phases comprise eight unique structure types, listed in Table I, that were used for solid solution modeling.

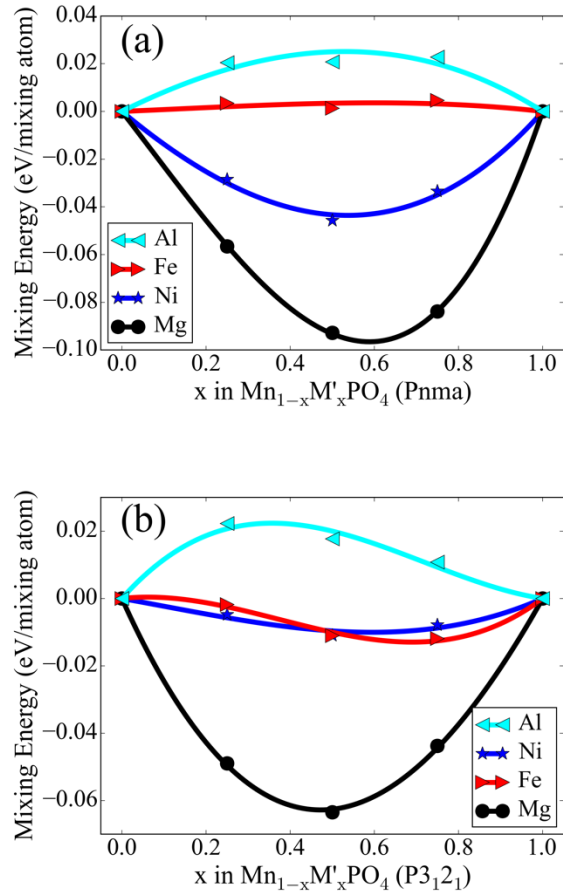
Table I. Crystal structures found on the DFT convex hulls and used for solid solution modeling.

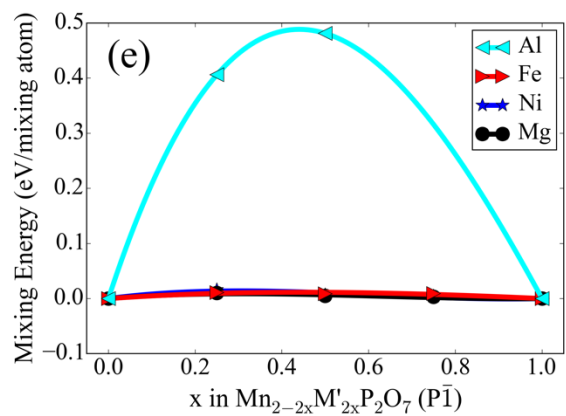
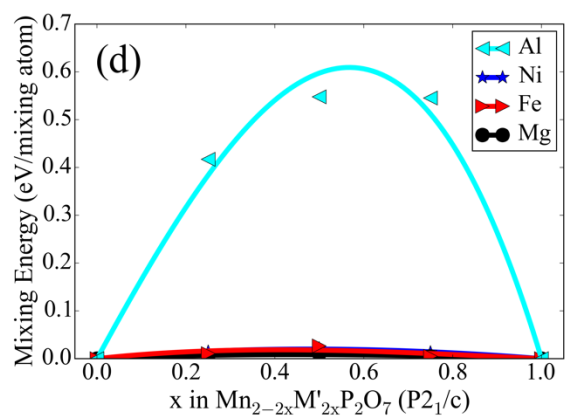
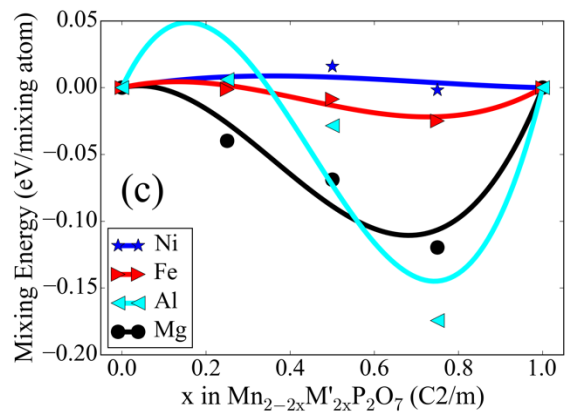
Stoichiometry	Space group	Phases on DFT convex hull
MPO_4	Pnma	MnPO_4
MPO_4	P3_12_1	FePO_4 , AlPO_4
$\text{M}_2\text{P}_2\text{O}_7$	C2/m	$\text{Mn}_2\text{P}_2\text{O}_7$, $\text{Mg}_2\text{P}_2\text{O}_7$
$\text{M}_2\text{P}_2\text{O}_7$	$\text{P2}_1/\text{c}$	$\text{Ni}_2\text{P}_2\text{O}_7$
$\text{M}_2\text{P}_2\text{O}_7$	$\text{P}\bar{1}$	$\text{Fe}_2\text{P}_2\text{O}_7$
$\text{M}_3\text{P}_2\text{O}_8$	$\text{P2}_1/\text{c}$	$\text{Fe}_3\text{P}_2\text{O}_8$
$\text{M}_3\text{P}_4\text{O}_{14}$	Pnma	$\text{Fe}_3\text{P}_4\text{O}_{14}$
$\text{M}_7\text{P}_6\text{O}_{24}$	$\text{P}\bar{1}$	$\text{Fe}_7\text{P}_6\text{O}_{24}$

Figure 1 shows DFT mixing energies (eV/mixing atom) for binary mixing of Mn with Fe, Ni, Al, and Mg in each solid solution phase. Figure 1 also includes the third-order Redlich-Kister polynomials, which were fit to the DFT energies. The regular and sub-regular mixing parameters for the Redlich-Kister polynomials are listed in Table II. Many mixed phases exhibit negative mixing energies, which indicates a favorable mixed solid solution phase, and can imply the existence of a stable, mixed-metal, ordered phase at low temperatures. However, no such ordered phases were found in the DFT databases. For example, olivine $\text{Mn}_{0.5}\text{Mg}_{0.5}\text{PO}_4$ exhibits a strong mixing energy relative to MnPO_4 and MgPO_4 end members; however, MgPO_4 is not a stable phase. The ground state phases at the $\text{Mn}_{0.5}\text{Mg}_{0.5}\text{PO}_4$ composition at room temperature

are MnPO_4 , $\text{Mg}_2\text{P}_2\text{O}_7$, and oxygen gas according to our calculated phase diagrams. These are the same ground state phases shown in the DFT databases. The $\text{Mn}_{2-2x}\text{Al}_{2x}\text{P}_2\text{O}_7$ (C2/m) polynomial fit is distorted due to the large instability of the $\text{Al}_2\text{P}_2\text{O}_7$ end-member, which decomposes to AlPO_4 , Al_2O_3 , and P. However, due to the large energy of the Al-rich $\text{Mn}_{2-2x}\text{Al}_{2x}\text{P}_2\text{O}_7$ phases, these phases do not appear in the calculated phase diagrams and do not affect oxygen evolution behavior.

Figure 1: SQS mixing energies (eV/mixing atom) and Redlich-Kister third-order polynomial fits for sub-regular solid solution models for all eight structure types given in Table I. Plots a-h respectively show phases MPO_4 (Pnma), MPO_4 (P3₁2₁), $\text{M}_2\text{P}_2\text{O}_7$ (C2/m), $\text{M}_2\text{P}_2\text{O}_7$ (P2₁/c), $\text{M}_2\text{P}_2\text{O}_7$ (P), $\text{M}_3\text{P}_2\text{O}_8$ (P2₁/c), $\text{M}_3\text{P}_4\text{O}_{14}$ (Pnma), and $\text{M}_7\text{P}_6\text{O}_{24}$ (P).





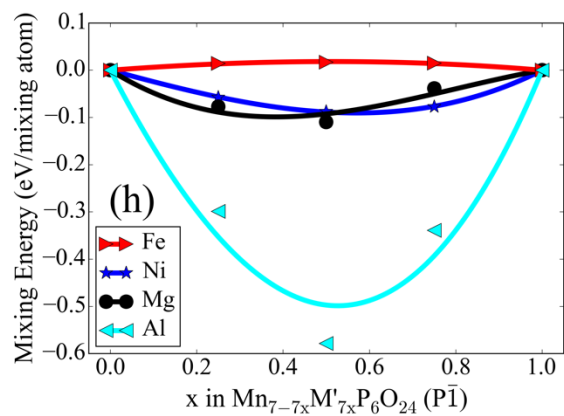
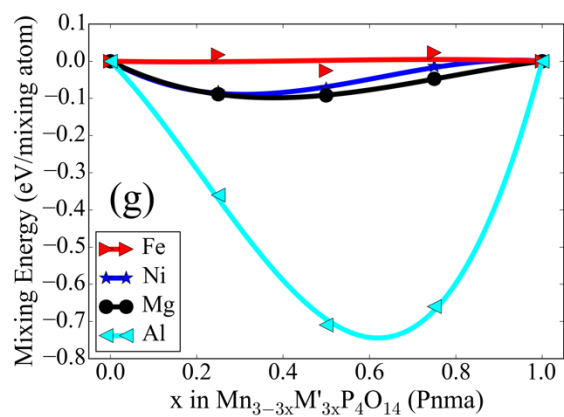
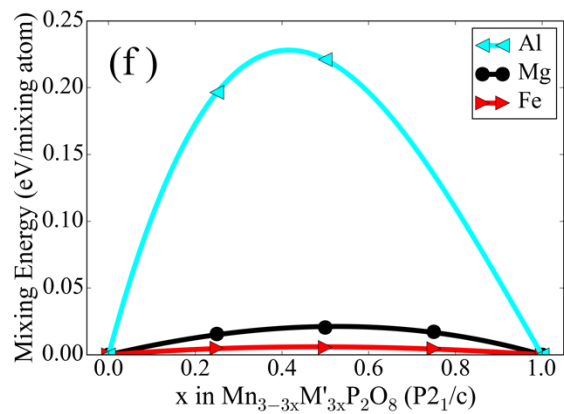


Table II. Regular (L_0) and sub-regular (L_1) solution parameters (eV/mixing atom) used in third-order Redlich-Kister polynomials for sub-regular solid solution models.

	$M' = \text{Fe}$		$M' = \text{Ni}$		$M' = \text{Al}$		$M' = \text{Mg}$	
	L_0	L_1	L_0	L_1	L_0	L_1	L_0	L_1
$\text{Mn}_{1-x}\text{M}'_x\text{PO}_4$ (Pnma)	0.014	0.006	-0.173	-0.026	0.100	0.012	-0.373	-0.146
$\text{Mn}_{1-x}\text{M}'_x\text{PO}_4$ (P3 ₁ 2 ₁)	-0.040	-0.054	-0.039	-0.016	0.080	-0.061	-0.250	0.028
$\text{Mn}_{2-2x}\text{M}'_{2x}\text{P}_2\text{O}_7$ (C2/m)	-0.053	-0.125	0.032	-0.024	-0.291	-0.962	-0.355	-0.426
$\text{Mn}_{2-2x}\text{M}'_{2x}\text{P}_2\text{O}_7$ (P2 ₁ /c)	0.071	-0.029	0.080	-0.007	2.389	0.684	0.033	-0.007
$\text{Mn}_{2-2x}\text{M}'_{2x}\text{P}_2\text{O}_7$ (P $\bar{1}$)	0.045	-0.010	0.042	-0.061	1.925	-0.481	0.027	-0.036
$\text{Mn}_{3-3x}\text{M}'_{3x}\text{P}_2\text{O}_8$ (P2 ₁ /c)	0.024	-0.002	--	--	0.884	-0.326	0.085	0.009
$\text{Mn}_{3-3x}\text{M}'_{3x}\text{P}_4\text{O}_{14}$ (Pnma)	0.008	0.032	-0.276	0.370	-2.776	-1.601	-0.365	0.218
$\text{Mn}_{7-7x}\text{M}'_{7x}\text{P}_6\text{O}_{24}$ (P $\bar{1}$)	0.074	0.004	-0.354	-0.105	-1.989	-0.214	-0.370	0.206

Figures 2-6 show our calculated phase diagrams for the binary systems of $\text{Mn}_{1-x}\text{M}'_x\text{PO}_4$ ($M' = \text{Fe, Ni, Al, Mg}$). For the Mn-Fe system, as described above, we report one phase diagram that excludes the quartz phase during energy minimization, and another phase diagram that includes the quartz phase. Coexistence regions are labeled by their phases. Solid phases with majority metals are written with those metals; for example, in Figure 1a, “ MnPO_4 ” is written to indicate a $\text{Mn}_{1-x}\text{Fe}_x\text{PO}_4$ phase containing a majority of Mn. Phases with no consistent majority metal are written with “M”; for example, “ MPO_4 ” is written to indicate a $\text{Mn}_{1-x}\text{Fe}_x\text{PO}_4$ region that exists continuously across majority Mn and majority Fe compositions. The quartz-free $\text{Mn}_{1-x}\text{Fe}_x\text{PO}_4$ phase diagram includes three distinct $\text{Mn}_2\text{P}_2\text{O}_7$ regions in the top left. These regions are too small for labels; they contain C2/m, C2/m+P $\bar{1}$, and P $\bar{1}$ phases from left to right. Due to this polymorphism, we label the $\text{Mn}_2\text{P}_2\text{O}_7$ phases in this phase diagram with their space groups.

We can use the phase diagram to understand oxygen evolution as a function of transition metal composition. Fe exhibits complete solubility in MnPO_4 at temperatures above 100 K. This Fe solubility stabilizes the $\text{Mn}_{1-x}\text{Fe}_x\text{PO}_4$ phase and increases the initial temperature of oxygen evolution. Ni, Al, and Mg exhibit low solubilities in MnPO_4 . For this reason, these

elements cannot be used to increase the temperature of the transition from MnPO_4 to $\text{Mn}_2\text{P}_2\text{O}_7$. However, Ni and Mg do exhibit considerable solubility in $\text{Mn}_2\text{P}_2\text{O}_7$, stabilizing the pyrophosphate, and allowing these elements to decrease the temperature of the transition from MnPO_4 to $\text{Mn}_2\text{P}_2\text{O}_7$.

Figure 2: $\text{Mn}_{1-x}\text{Fe}_x\text{PO}_4$ phase diagram excluding the quartz-type (P3_12_1) FePO_4 phase during energy minimization. This phase diagram was calculated using Thermo-Calc with DFT-derived sub-regular solution models for each solid phase. All MPO_4 phases form the Pnma space group. O_2 gas is considered at one bar of pressure.

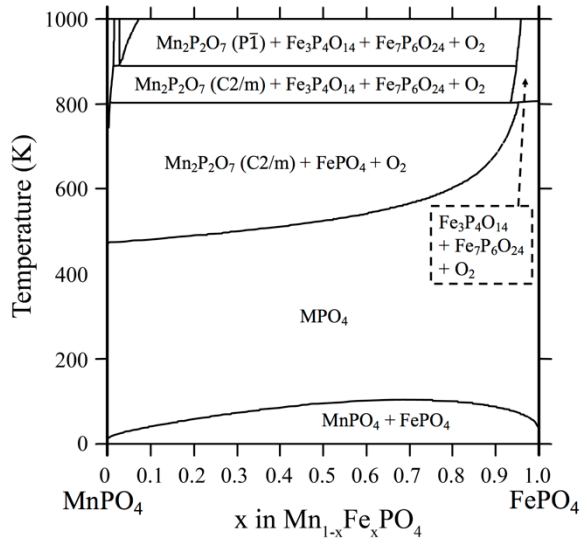


Figure 3: $\text{Mn}_{1-x}\text{Fe}_x\text{PO}_4$ phase diagram including the quartz-type (P3_12_1) FePO_4 phase during energy minimization. This phase diagram was calculated using Thermo-Calc with DFT-derived sub-regular solution models for each solid phase. MnPO_4 , FePO_4 , and $\text{Mn}_2\text{P}_2\text{O}_7$ phases form the Pnma , P3_12_1 , and C2/m space groups respectively. O_2 gas is considered at one bar of pressure.

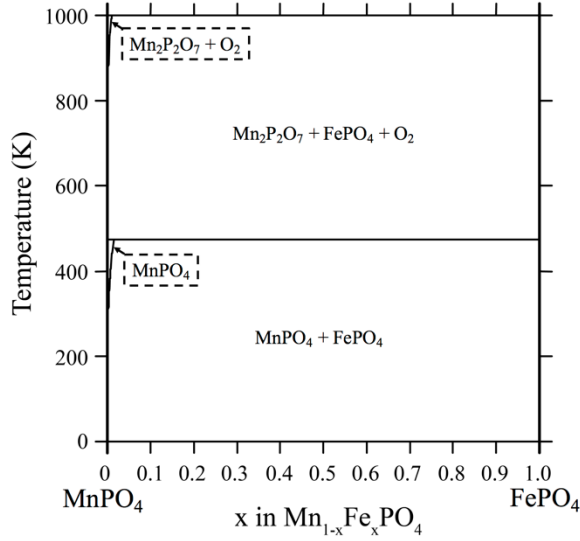


Figure 4: $\text{Mn}_{1-x}\text{Ni}_x\text{PO}_4$ phase diagram, calculated using Thermo-Calc with DFT-derived sub-regular solution models for each solid phase. MnPO_4 , $\text{Mn}_2\text{P}_2\text{O}_7$, and $\text{Ni}_2\text{P}_2\text{O}_7$ phases form the Pnma , C2/m , and $\text{P2}_1/\text{c}$ space groups respectively. O_2 gas is considered at one bar of pressure.

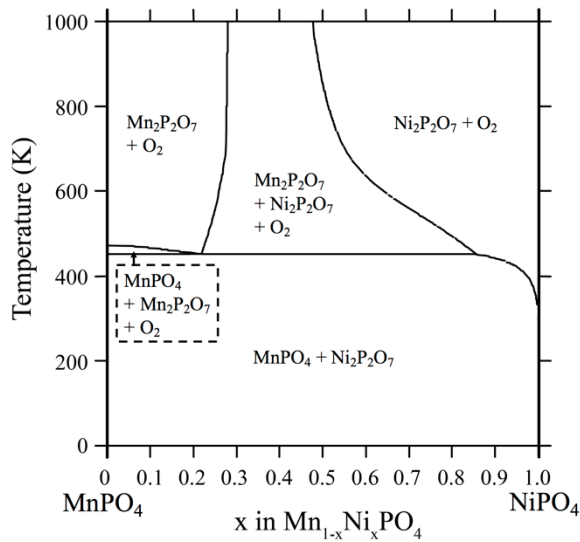


Figure 5: $\text{Mn}_{1-x}\text{Mg}_x\text{PO}_4$ phase diagram, calculated using Thermo-Calc with DFT-derived sub-regular solution models for each solid phase. MnPO_4 forms the Pnma space group, and all $\text{M}_2\text{P}_2\text{O}_7$ phases form the C2/m space group. O_2 gas is considered at one bar of pressure.

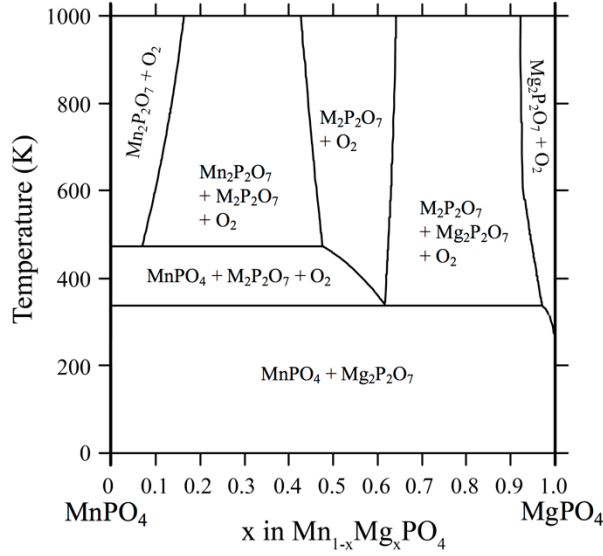
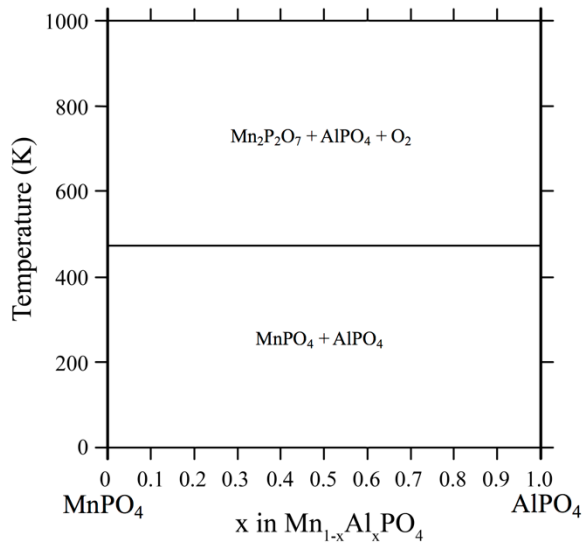


Figure 6: $\text{Mn}_{1-x}\text{Al}_x\text{PO}_4$ phase diagram, calculated using Thermo-Calc with DFT-derived sub-regular solution models for each solid phase. MnPO_4 , AlPO_4 , and $\text{Mn}_2\text{P}_2\text{O}_7$ phases form the Pnma, P3_12_1 , and C2/m space groups respectively. O_2 gas is considered at one bar of pressure.



Figures 7-11 show oxygen evolution (δ) and mass retention for $\text{Mn}_{1-x}\text{M}'_x\text{PO}_4$ ($\text{M}' = \text{Fe}, \text{Ni}, \text{Al}, \text{Mg}$) materials as a function of temperature. These plots illustrate how transition metal mixing affects pure MnPO_4 in terms of both the T_{O_2} and δ . Figure 7 shows oxygen evolution for the Mn-Fe system excluding the quartz-type FePO_4 phase. The effect of Fe mixing on T_{O_2} is relatively modest. From 0% Fe to 50% Fe, each 10% increment of Fe mixing achieves a 10 K increase in T_{O_2} . Therefore, T_{O_2} increases from 480 K to just 530 K by adding 50% Fe. However, the effect of Fe mixing on δ and corresponding mass retention is substantial. Pure MnPO_4 loses 5.3% of its mass at temperatures above 480 K. When Fe is added, mass retention is greatly improved at elevated temperatures. $\text{Mn}_{0.5}\text{Fe}_{0.5}\text{PO}_4$ loses just 2.0% of its mass at 600 K and still just 2.5% at 800 K. At 570 (300 °C), $\text{Mn}_{0.5}\text{Fe}_{0.5}\text{PO}_4$ δ is decreased by 70% relative to MnPO_4 . This improvement in mass retention could decrease the amount of heat generated through electrolyte combustion during thermal runaway and thereby improve safety. The addition of smaller amounts of Fe also can provide some safety benefit. For example, the addition of 30% Fe limits oxygen evolution to 3.1% of mass at 570 K.

Figure 7: Oxygen evolution (a) and mass retention (b) diagrams for $\text{Mn}_{1-x}\text{Fe}_x\text{PO}_4$ delithiated cathode materials excluding the quartz-type (P3_12_1) FePO_4 phase during energy minimization. Oxygen evolution (δ) is expressed relative to the system composition of $\text{MPO}_{4-\delta}$. Reaction products are the equilibrium phases shown in the phase diagram in Figure 2. Mass retention is expressed as a percentage of the mass of the $\text{Mn}_{1-x}\text{Fe}_x\text{PO}_4$.

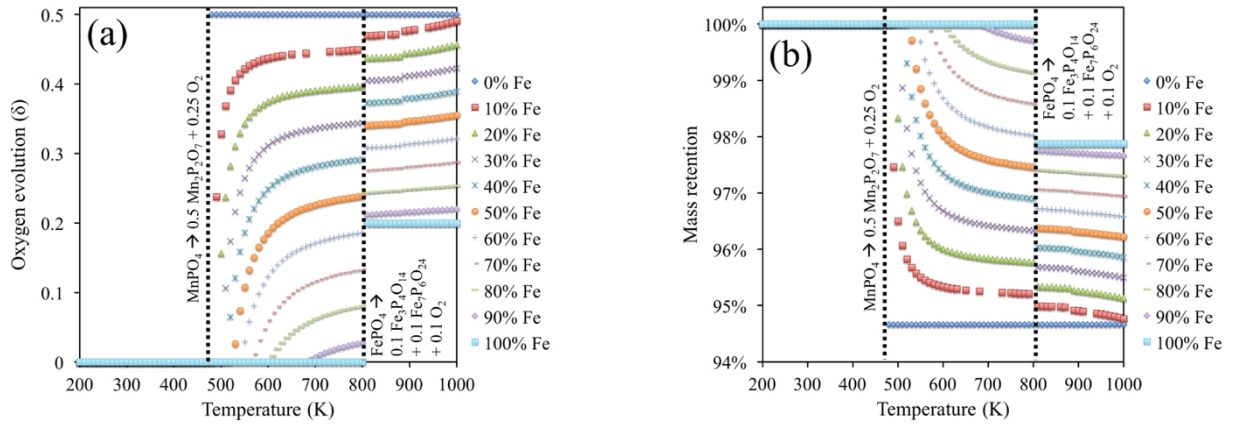


Figure 8: Oxygen evolution (a) and mass retention (b) diagrams for $\text{Mn}_{1-x}\text{Fe}_x\text{PO}_4$ delithiated cathode materials including the quartz-type (P3_12_1) FePO_4 phase during energy minimization. Oxygen evolution (δ) is expressed relative to the system composition of $\text{MPO}_{4-\delta}$. Reaction products are the equilibrium phases shown in the phase diagram in Figure 3. Mass retention is expressed as a percentage of the mass of the $\text{Mn}_{1-x}\text{Fe}_x\text{PO}_4$.

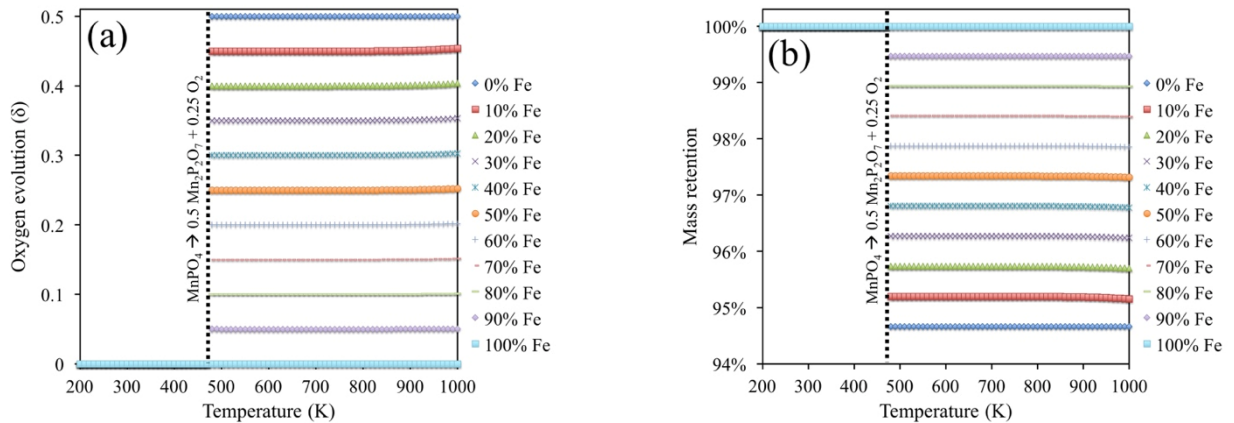


Figure 9: Oxygen evolution (a) and mass retention (b) diagrams for $\text{Mn}_{1-x}\text{Ni}_x\text{PO}_4$ delithiated cathode materials. Oxygen evolution (∂) is expressed relative to the system composition of $\text{MPO}_{4-\partial}$. Reaction products are the equilibrium phases shown in the phase diagram in Figure 4. Mass retention is expressed as a percentage of the mass of the $\text{Mn}_{1-x}\text{Ni}_x\text{PO}_4$.

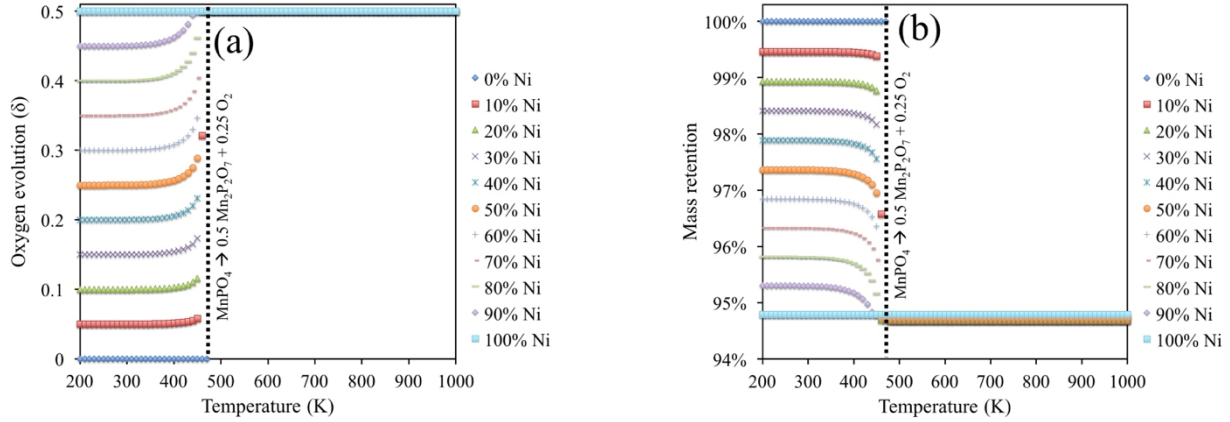


Figure 10: Oxygen evolution (a) and mass retention (b) diagrams for $\text{Mn}_{1-x}\text{Mg}_x\text{PO}_4$ delithiated cathode materials. Oxygen evolution (∂) is expressed relative to the system composition of $\text{MPO}_{4-\partial}$. Reaction products are the equilibrium phases shown in the phase diagram in Figure 5. Mass retention is expressed as a percentage of the mass of the $\text{Mn}_{1-x}\text{Mg}_x\text{PO}_4$.

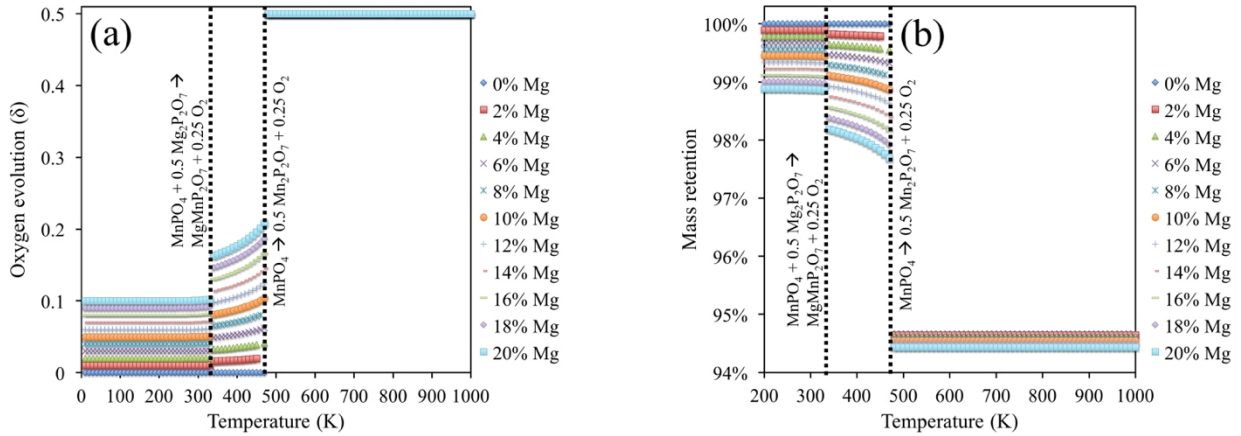
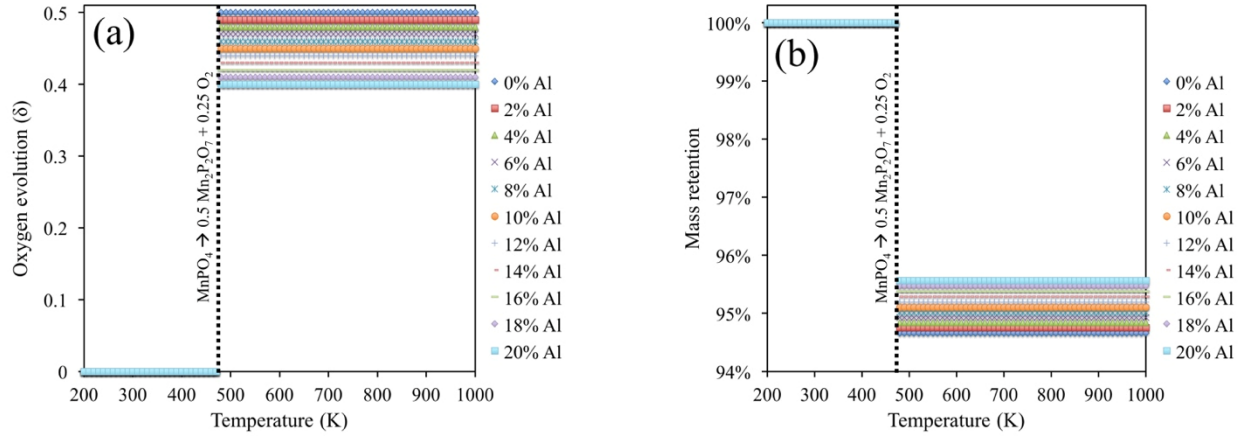


Figure 11: Oxygen evolution (a) and mass retention (b) diagrams for $\text{Mn}_{1-x}\text{Al}_x\text{PO}_4$ delithiated cathode materials. Oxygen evolution (δ) is expressed relative to the system composition of $\text{MPO}_{4-\delta}$. Reaction products are the equilibrium phases shown in the phase diagram in Figure 6. Mass retention is expressed as a percentage of the mass of the $\text{Mn}_{1-x}\text{Al}_x\text{PO}_4$.



Addition of Al to MnPO_4 does not affect T_{O_2} because there is no solubility of Al in MnPO_4 or $\text{Mn}_2\text{P}_2\text{O}_7$. For $\text{Mn}_{1-x}\text{Al}_x\text{PO}_4$ cathodes, δ is decreased only in proportion to the Al concentration. However, the Al concentration in a cathode must be kept small because Al is redox inactive and decreases cathode capacity. Therefore, Al substitution is not a promising strategy for controlling oxygen evolution.

NiPO_4 and MgPO_4 are not stable at room temperature and decompose into $\text{Ni}_2\text{P}_2\text{O}_7$ and $\text{Mg}_2\text{P}_2\text{O}_7$ respectively along with oxygen gas. Addition of Ni or Mg to MnPO_4 decreases the initial temperature of oxygen evolution down to at most 90 K, which is the condensation point for oxygen gas and is therefore the low-temperature limit of our oxygen gas evolution model. Therefore, $\text{Mn}_{1-x}\text{Ni}_x\text{PO}_4$ and $\text{Mn}_{1-x}\text{Mg}_x\text{PO}_4$ materials can evolve oxygen gas even at room temperature granted sufficient kinetics or time to allow nucleation of the $\text{M}_2\text{P}_2\text{O}_7$ phases. For Ni

and Mn substitution, δ at temperatures below 400 K is increased in proportion to substitution for Mn. For Ni and Mg substitution, δ around 400 K is increased above the proportion of substitution for Mn due to the formation of mixed $M_2P_2O_7$ phases. This phenomenon is especially pronounced for Mg due to a $Mn_{2-2x}Mg_{2x}P_2O_7$ phase around $x = 0.5$ that is stable at 340 K. These mixed $M_2P_2O_7$ phases stabilize the reaction products for oxygen evolution and make oxygen evolution more favorable at lower temperatures. The addition of Ni or Mg to $MnPO_4$ therefore exacerbates the safety risk of thermal runaway. In summary, of all substitutions considered, Mg has the most detrimental effect for safety, followed by Ni. Al has a small positive affect on safety, and Fe has the greatest positive affect on safety.

Fe mixing in olivine $Mn_{1-x}Fe_xPO_4$ improves safety because Fe stabilizes $MnPO_4$ relative to $Mn_2P_2O_7$. To further improve the oxygen evolution behavior of $MnPO_4$, other elements should be sought that can stabilize oxygen evolution reactants relative to reaction products. These elements should be relatively more stable in the M^{3+} chemical environment of $MnPO_4$ and relatively less stable in the M^{2+} chemical environment of $Mn_2P_2O_7$. The Jahn-Teller distortion of $MnPO_4$ may complicate this search, as certain 3+ metals such as Al may not be energetically favorable in the distorted $MnPO_4$ crystal structure.⁵² Such metals would not stabilize $MnPO_4$ but would rather phase separate as in the case of $AlPO_4$.

IV. SUMMARY

$LiMnPO_4$ is a promising cathode material; however, oxygen evolution from the delithiated $MnPO_4$ phase facilitates thermal runaway and jeopardizes safety. Delithiated cathode materials that form inside batteries are difficult to characterize experimentally. We used density functional theory calculations to study oxygen evolution from $Mn_{1-x}M'_xPO_4$ ($M' = Fe, Ni, Al$,

Mg) delithiated cathode materials. We calculated the effect of transition metal mixing on both the initial temperature of oxygen evolution (T_{O_2}) during heating and the cumulative amount of oxygen evolution (δ) at a given temperature. We find that Fe mixing in $MnPO_4$ increases T_{O_2} , and also decreases δ . Addition of Al does not change T_{O_2} but can slightly decrease δ . Mixing of Ni or Mg decreases T_{O_2} and thereby worsens the safety risk associated with oxygen evolution. Understanding this relationship between transition metal mixing and oxygen evolution can facilitate simultaneous optimization of safety and other performance characteristics. Further work is suggested to identify other metals besides Fe that can stabilize $MnPO_4$ relative to $Mn_2P_2O_7$ and other oxygen evolution reaction products.

ACKNOWLEDGEMENTS

The authors are grateful to James Saal and Dana Frankel for discussions regarding CALPHAD, and to Antoine Emery for editing. The authors acknowledge support from the Center for Electrochemical Energy Science (CEES), an Energy Frontier Research Center (EFRC) funded by the U.S. Department of Energy, Office of Science, Office of Basic Energy Sciences (Award No. DE-AC02-06CH11357). D.S. also acknowledges fellowship support from Northwestern's Hierarchical Materials Cluster Program and from the Institute for Sustainability and Energy at Northwestern (ISEN). This research used resources of the National Energy Research Scientific Computing Center, which is supported by the Office of Science of the U.S. Department of Energy under Contract No. DE-AC02-05CH11231 as well as the Northwestern University Quest computing resources.

APPENDIX: THERMO-CALC SETTINGS

Within Thermo-Calc, we turned on the “global minimization” parameter for accuracy, and left all other parameters in their default states. In some regions of the phase diagrams, Thermo-Calc indicated the existence of phases with phase fractions below 10^{-9} . We assumed these phases either were present due to numerical errors or were inconsequential for properties of interest. We therefore removed these phases and their associated phase boundaries in regions where they appeared with phase fractions below 10^{-9} . We retained these phases in regions where they appeared with phase fractions above 10^{-9} , and in these regions, the maximum phase fractions ranged between 10^{-2} and unity.

REFERENCES

- ¹ J.B. Goodenough and Y. Kim, *Chem. Mater.* **22**, 587 (2010).
- ² C. Delacourt, P. Poizot, J.-M. Tarascon, and C. Masquelier, *Nat. Mater.* **4**, 254 (2005).
- ³ Y. Song, P.Y. Zavalij, M. Suzuki, and M.S. Whittingham, *Inorg. Chem.* **41**, 5778 (2002).
- ⁴ K. Zaghib, M. Dontigny, A. Guerfi, P. Charest, I. Rodrigues, A. Mauger, and C.M. Julien, *J. Power Sources* **196**, 3949 (2011).
- ⁵ T. Muraliganth and A. Manthiram, *J. Phys. Chem. C* **114**, 15530 (2010).
- ⁶ V. Aravindan, J. Gnanaraj, Y.-S. Lee, and S. Madhavi, *J. Mater. Chem. A* **1**, 3518 (2013).
- ⁷ A. Yamada, Y. Kudo, and K.-Y. Liu, *J. Electrochem. Soc.* **148**, A1153 (2001).
- ⁸ G. Li, H. Azuma, and M. Tohda, *Electrochem. Solid-State Lett.* **5**, A135 (2002).
- ⁹ G. Chen and T.J. Richardson, *J. Power Sources* **195**, 1221 (2010).
- ¹⁰ S.-W. Kim, J. Kim, H. Gwon, and K. Kang, *J. Electrochem. Soc.* **156**, A635 (2009).
- ¹¹ J. Yoshida, S. Nakanishi, H. Iba, H. Abe, and M. Naito, *Int. J. Appl. Ceram. Technol.* **10**, 764 (2013).
- ¹² I. Belharouak, W. Lu, J. Liu, D. Vissers, and K. Amine, *J. Power Sources* **174**, 905 (2007).
- ¹³ J. Kim, K.-Y. Park, I. Park, J.-K. Yoo, J. Hong, and K. Kang, *J. Mater. Chem.* **22**, 11964 (2012).
- ¹⁴ G.M. Nolis, F. Omenya, R. Zhang, B. Fang, S. Upreti, N.A. Chernova, F. Wang, J. Graetz, Y.-Y. Hu, C.P. Grey, and M.S. Whittingham, *J. Mater. Chem.* **22**, 20482 (2012).
- ¹⁵ J. Hafner, C. Wolverton, and G. Ceder, *MRS Bulletin* **31**, 659 (2006).
- ¹⁶ R. Malik, A. Abdellahi, and G. Ceder, *J. Electrochem. Soc.* **160**, A3179 (2013).
- ¹⁷ J.E. Saal, S. Kirklin, M. Aykol, B. Meredig, and C. Wolverton, *Jom* **65**, 1501 (2013).
- ¹⁸ D.H. Snyder, M. Aykol, S. Kirklin, and C. Wolverton, *J. Electrochem. Soc.* **163**, A2054 (2016).
- ¹⁹ C. Wolverton and A. Zunger, *Phys. Rev. B* **57**, 2242 (1998).
- ²⁰ C. Wolverton and A. Zunger, *Phys. Rev. Lett.* **81**, 606 (1998).

- ²¹ C. Wolverton and A. Zunger, J. Electrochem. Soc. **145**, 2424 (1998).
- ²² J. Reed, G. Ceder, and A. Van der Ven, Electrochem. Solid-State Lett. **4**, A78 (2001).
- ²³ R.I. Eglitis and G. Borstel, Phys. Stat. Sol. (a) **202**, R13 (2005).
- ²⁴ R.I. Eglitis, Phys. Scr. **90**, 094012 (2015).
- ²⁵ S.P. Ong, A. Jain, G. Hautier, B. Kang, and G. Ceder, Electrochem. Commun. **12**, 427 (2010).
- ²⁶ G. Kresse and J. Hafner, Phys. Rev. B **47**, 558 (1993).
- ²⁷ G. Kresse and J. Hafner, Phys. Rev. B **49**, 14251 (1994).
- ²⁸ G. Kresse and J. Furthmüller, Comput. Mater. Sci. **6**, 15 (1996).
- ²⁹ G. Kresse and J. Furthmüller, Phys. Rev. B **54**, 11169 (1996).
- ³⁰ P.E. Blöchl, Phys. Rev. B **50**, 17953 (1994).
- ³¹ G. Kresse and D. Joubert, Phys. Rev. B **59**, 1758 (1999).
- ³² J. Perdew, K. Burke, and M. Ernzerhof, Phys. Rev. Lett. **77**, 3865 (1996).
- ³³ V.I. Anisimov, J. Zaanen, and O.K. Andersen, Phys. Rev. B **44**, 943 (1991).
- ³⁴ V. Anisimov, I. Solovyev, M. Korotin, M. Czyżyk, and G. Sawatzky, Phys. Rev. B **48**, 16929 (1993).
- ³⁵ A. Liechtenstein, V. Anisimov, and J. Zaanen, Phys. Rev. B **52**, 5467 (1995).
- ³⁶ S.L. Dudarev, G.A. Botton, S.Y. Savrasov, C.J. Humphreys, and A. Sutton, Phys. Rev. B **57**, 1505 (1998).
- ³⁷ L. Wang, T. Maxisch, and G. Ceder, Phys. Rev. B **73**, 195107 (2006).
- ³⁸ S. Kirklin, J.E. Saal, B. Meredig, A. Thompson, J.W. Doak, M. Aykol, S. Rühl, and C. Wolverton, Npj Comp. Mater. **1**, 1 (2015).
- ³⁹ A. Zunger, S.H. Wei, L.G. Ferreira, and J.E. Bernard, Phys. Rev. Lett. **65**, 353 (1990).
- ⁴⁰ A. van de Walle, P. Tiwary, M. de Jong, D.L. Olmsted, M. Asta, A. Dick, D. Shin, Y. Wang, L.Q. Chen, and Z.K. Liu, CALPHAD: Comput. Coupling Phase Diagrams Thermochem. **42**, 13 (2013).
- ⁴¹ D.H. Snyder and C. Wolverton, J. Phys. Chem. C **120**, 5932 (2016).
- ⁴² J.E. Saal, S. Kirklin, M. Aykol, B. Meredig, and C. Wolverton, Jom **65**, 1501 (2013).
- ⁴³ A. Jain, S.P. Ong, G. Hautier, W. Chen, W.D. Richards, S. Dacek, S. Cholia, D. Gunter, D. Skinner, G. Ceder, and K.A. Persson, APL Mater. **1**, 011002 (2013).
- ⁴⁴ S.P. Ong, L. Wang, B. Kang, and G. Ceder, Chem. Mater. **20**, 1798 (2008).
- ⁴⁵ A. Jain, G. Hautier, S.P. Ong, C.J. Moore, C.C. Fischer, K.A. Persson, and G. Ceder, Phys. Rev. B **84**, 0451151 (2011).
- ⁴⁶ M.W. Chase, C.A. Davies, J.F. Downey, D.J. Frurip, R.A. McDonald, and A.N. Syverud, *National Institute of Standards and Technology: JANAF Thermochemical Tables* (1985).
- ⁴⁷ C.-Y. Jhu, Y.-W. Wang, C.-Y. Wen, and C.-M. Shu, Applied Energy **100**, 127 (2012).
- ⁴⁸ S. Grindy, B. Meredig, S. Kirklin, J.E. Saal, and C. Wolverton, Phys. Rev. B **87**, 075150 (2013).
- ⁴⁹ J.O. Andersson, T. Helander, L. Höglund, and P. Shi, CALPHAD: Comput. Coupling Phase Diagrams Thermochem. **26**, 273 (2002).
- ⁵⁰ H.N. Ng and C. Calvo, Canadian Journal of Chemistry **53**, 2064 (1975).
- ⁵¹ M. Dontigny, A. Guerfi, J. Trottier, J. Hamel-Paquet, V. Gariepy, K. Galoutov, P. Hovington, A. Mauger, H. Groult, and C.M. Julien, J. Power Sources **216**, 192 (2012).
- ⁵² A. Yamada and S.C. Chung, J. Electrochem. Soc. **148**, A960 (2001).